Custom Over-the-air Scalable mmWave Testbed for Fast TTD-based Rainbow Beam Training

Mohammad Ali Mokri[†,1], Yen-Chin Wang[†,2], Ruifu Li[2], Aditya Wadaskar[2], Subhanshu Gupta[1], Deukhyoun Heo[1], and Danijela Cabric[2]
[1]School of Electrical Engineering and Computer Science, Washington State University, WA, USA
[2]Department of Electrical and Computer Engineering, University of California, Los Angeles, CA, USA
Email: m.mokri@wsu.edu, {ycwang85, doanr37, adityaw}@ucla.edu, dheo@wsu.edu, sgupta@eecs.wsu.edu, danijela@ee.ucla.edu

***Abstract*—Millimeter-wave (mmWave) systems require a large number of antennas, which makes the beam training challenging and time-consuming for conventional phased arrays. Recently, a true-time-delay (TTD) array-based beam training algorithm has been shown as an effective solution to overcome the training overhead in large arrays. In this paper, we present a custom-built over-the-air (OTA) testbed to study the effects of hardware impairments on the TTD-based beam training and verify its feasibility in a real system. We proposed an orthogonal matching pursuit (OMP) based reconstruction algorithm along with a phase calibration dictionary to combat nonidealities such as strong frequency selectivity and phase misalignment in the received raw IQ signal. Post-processing results showed that with the nonideality effects properly handled, the 3D TTD beam training algorithm can achieve high AOA estimation accuracy.**

***Keywords*—Planar arrays, true-time-delay arrays, 3D beam training, OTA testing**

I. Introduction

Abundant spectrum allocated for millimeter wave (mmWave) communication enables multi-Gbps transmission speeds per user in 5G & beyond networks [1]. Due to the large propagation loss at mmWave frequencies, a large number of antenna elements are needed to ensure the receiver achieves a high beamforming gain. However, the large antenna array, together with the narrow beam, makes the beam training challenging and time-consuming for conventional phased arrays. Recently, a frequency-dependent beam training algorithm [2] [3] using true-time-delay (TTD) based antenna arrays [4] was proposed to serve as a promising candidate for fast beam training. This technique can simultaneously probe multiple directions in a single orthogonal frequency division multiplexing (OFDM) symbol, which greatly shortens the required time for beam training. Some preliminary simulation and experimental results have been reported in [5] [6].

This work presents a custom over-the-air (OTA) testbed to study the effects of hardware impairments on the TTD-based beam training at mmWave and demonstrate the efficacy of fast rainbow beam training leveraging TTD. The custom testbed integrated commercial off-the-shelf (COTS) components, including data generation and acquisition using Xilinx ZCU111, mmWave front-end (ADI ADAR2004), mmWave oscillators (ADI ADF4372) together with planar custom-designed patch antenna array. The custom testbed provides raw in-phase/quadrature-phase (IQ) data from each antenna to the data acquisition unit for further post-processing.

Measurement results demonstrated non-idealities in the received raw IQ data not covered earlier in the prior works by authors on fast TTD beam training. These effects include but are not limited to strong frequency selectivity induced by echos/reflections and phase misalignment across antenna elements. To overcome these nonidealities, we propose an orthogonal matching pursuit (OMP) based reconstruction algorithm to remove the multipath effect in the received raw IQ. Moreover, we built a phase calibration dictionary to compensate for the phase misalignment in each capture. Post-processing results showed that after the nonideality effects were properly handled, the TTD beam training algorithm could achieve high AOA estimation accuracy in our mmWave OTA testbed.

The rest of this paper is organized as follows. Section II briefly reviews the design and algorithm of the TTD-based beam training. The design and integration of the OTA testbed are presented in Section III. Section IV describes the signal processing & calibration process on the received raw IQ. Section V contains the measured results and discussions, followed by conclusions in Section V.

Notation: Boldfaced lower-case letters denote column vectors and boldfaced upper-case letters denote matrices. The symbols $\mathbf{A}^T$, $\mathbf{A}^*$, and $\mathbf{A}^\dagger$ denote the transpose, the complex conjugate, and the conjugate-transpose of matrix $\mathbf{A}$ respectively. The element in i-th row and j- column in matrix $\mathbf{A}$ is denoted by $\{\mathbf{A}\}_{i,j}$. The L-2 norm of a vector $\mathbf{v}$ is denoted by $||\mathbf{v}||$.

II. Review of True-Time-Delay Based Fast Beam Training

In this section, we briefly review the TTD-based beam training design and algorithm. Figure 1 shows the architecture of a receiver that is equipped with a 2D TTD array. Here, we consider a uniform planar array with N antenna elements arranged in an $N_{az} \times N_{el}$ array, where N_{az} and N_{el} are the number of antenna in the azimuth and elevation dimension of the array, respectively. $\phi_{(n_{az},n_{el})}$ is the phase shift on each antenna element. Compared with the conventional phased array, an additional time delay $\tau_{(n_{az},n_{el})}$ is introduced for each antenna element.

This work was supported by the National Science Foundation (NSF) under Grant 1955306.

The dagger-ed authors, Mohammad Ali Mokri[†,1] and Yen-Chin Wang[†,2], contributed equally to this paper.

ICC 2024 - IEEE International Conference on Communications | 978-1-7281-9054-9/24/$31.00 ©2024 IEEE | DOI: 10.1109/ICC51166.2024.10622779

In our previous work [5], we showed that a uniform planar TTD array with an OFDM system of M subcarriers can be used for fast 3D beam training enabling complete spherical coverage using element-level delay compensation ($\tau_{(n_{az},n_{el})}$). Besides, in [7], we proposed a dictionary-based fast-beam training algorithm for a better resolution of AOA estimation. In the following, we briefly summarize the 3D beam training design and the dictionary-based algorithm for the consistency and completeness of the paper. The design and algorithm were adopted in our OTA experiment setup and post-data processing.

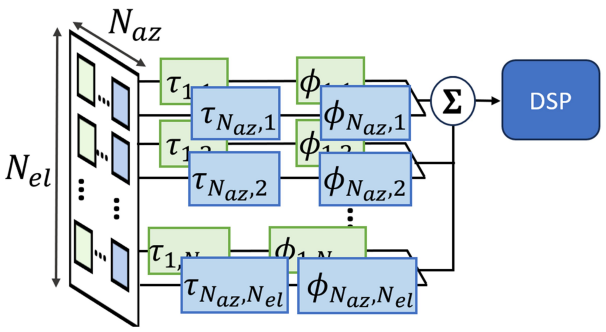

Fig. 1. Architecture of a 2D TTD array

A. TTD Beam Training Design

We consider uniformly spaced delay in each dimension of the 2D TTD array with spacings $\Delta\tau_{az}$ and $\Delta\tau_{el}$. The accumulated delay at each antenna element is the sum of the delay corresponding to the azimuth and elevation, i.e., $\tau_{(n_{az},n_{el})} = (n_{az}-1)\Delta\tau_{az} + (n_{el}-1)\Delta\tau_{el}$. With the additional delays, the beam direction of each subcarrier of a wideband OFDM get dispersed. In the TTD-based beam training, we would like to have each subcarrier of an OFDM symbol get beamed toward different directions, so that we can greatly shorten the beam training overhead [8]. The goal of the design is to determine the delay spacings and number of subcarriers used for beam training pilots to achieve full spherical coverage of codebook beams across the angular domain.

In [5], we have shown that a planar TTD array with $\Delta\tau_{el} = \frac{b}{BW}$ for coverage factor $b \in (0,1]$ and $\Delta\tau_{az} = k\Delta\tau_{el}$ can realize a 3D beam training that scans the angular range $\theta_{az} \in [-\pi/2, \pi/2]$ and $\theta_{el} \in [(1-b)\pi/2, \pi-(1-b)\pi/2]$. For a 2×2 array which was adopted in the OTA experiment in this paper, we chose $k=4$ and $b=0.5$ to cover the angular range $[-\pi/4, 3\pi/4]$ in elevation direction with proper beamwidth.

B. Dictionary-based Beam Training Algorithm

Given a $\tau_{(n_{az},n_{el})}$ design, the equivalent TTD array combiner at the m-th OFDM subcarrier, denoted as $\mathbf{w}(f_m)$, is determined. The n-th element of the corresponding TTD array combiner can be expressed as

$$[\mathbf{w}(f_m)]_n = \exp(j2\pi f_m \tau_{(n_{az},n_{el})}), \tag{1}$$

where $n = n_{az} + (n_{el}-1)N_{el}$. The dictionary-based beam training algorithm in [7] first generates a dictionary that collects the theoretical array gain across all OFDM subcarriers from different $(\theta_{az}, \theta_{el})$ candidates. Then, it finds the $(\hat{\theta}_{az}, \hat{\theta}_{el})$ candidate whose theoretical array gain matches the received power across all subcarriers best. A brief summary of the algorithm is described in the algorithm table.

Algorithm Dictionary-based Beam training

1: Generate the theoretical array gain dictionary $\mathbf{B} \in \mathbb{C}^{M\times Q_a Q_e}$. The element of $\mathbf{B}$ is defined as

$$\{\mathbf{B}\}_{(m,i)} = |\mathbf{w}(f_m)^H \mathbf{a}(\theta_{n_{az}(i)}, \theta_{n_{el}(i)}, f_m)|^2, \tag{2}$$

where $\mathbf{a}(\theta_{az}, \theta_{el}, f_m)$ is the array response at the m-th OFDM subcarrier with incident AOA pair $(\theta_{az}, \theta_{el})$. $\theta_{n_{az}(i)}$ and $\theta_{n_{el}(i)}$ are AOA candidates in the dictionary and are indexed by $n_{az}(i) = 1, 2, \cdots, Q_a$ and $n_{el}(i) = 1, 2, \cdots, Q_e$

2: Measure the received power across all subcarriers and formulate the vector $\mathbf{p} \in \mathbb{C}^{M\times 1}$.

3: Perform AOA estimation by checking the correlation between the measured $\mathbf{p}$ and the dictionary $\mathbf{B}$.

$$(\hat{\theta}_{az}, \hat{\theta}_{el}) = (\theta_{n_{az}(\hat{q}-\lfloor \frac{\hat{q}}{Q_a} \rfloor)}, \theta_{n_{el}(\lfloor \frac{\hat{q}}{Q_a} \rfloor+1)}), \tag{3}$$

where $\hat{q} = \arg\max_q \frac{\mathbf{p}^H [\mathbf{B}]_{(:,q)}}{||[\mathbf{B}]_{(:,q)}||^2}$

III. Overview of Custom OTA TTD Testbed

This section presents the custom mmWave TTD array testbed. Figure 2 shows the block diagram of the proposed testbed comprising four receivers (RX) and a transmit (TX) channel operating at 28GHz. In contrast to existing testbeds recently demonstrated over different frequency bands and applications [9]–[12], the proposed testbed can emulate delay compensation in either digital or analog baseband (after downconversion) as well as enable elemental beamforming with access to frequency downconverted data.

Figure 1 shows the architecture of a planar TTD array with each receiving channel comprising of a phase shifter and a delay compensating element. Additionally, no phase alignment and summation are performed at RF, enabling delay compensation post downconversion in the digital baseband. Following subsections describe each component of the testbed.

A. Transmitter

The 28 GHz TX comprises of 2 quadrature digital-to-analog converter (DAC) on Xilinx RFSoC (ZCU111), an image-reject upconversion mixer (ADMV1013), a LO synthesizer, an amplifier, and a high gain horn antenna ($\approx$ 20dBi). Key design considerations of the mmWave TX include high image rejection and linearity without any compression from the TX. Two 14-bit high-speed DACs on the ZCU111 generate the in-phase (I) and quadrature-phase (Q) signals (DAC and ADC sampling rates limited to 3932.16 GHz in the multi-tile synchronization mode). The quadrature DAC outputs are applied to ADMV1013 which upconvert them to mmWave when mixed with the local oscillator (LO) tone. This up-converter has two modes of operation: Baseband (BB) and IF. In this implementation, IF mode has been chosen; therefore, the BB digital signal is first upconverted to an IF equal to 950MHz using the digital upconverter inside the ZCU111. IF low-pass filters are placed at the DAC outputs to reduce the spur amplitude and aliases. The image-reject mixer allows phase and amplitude adjustment, resulting in high image

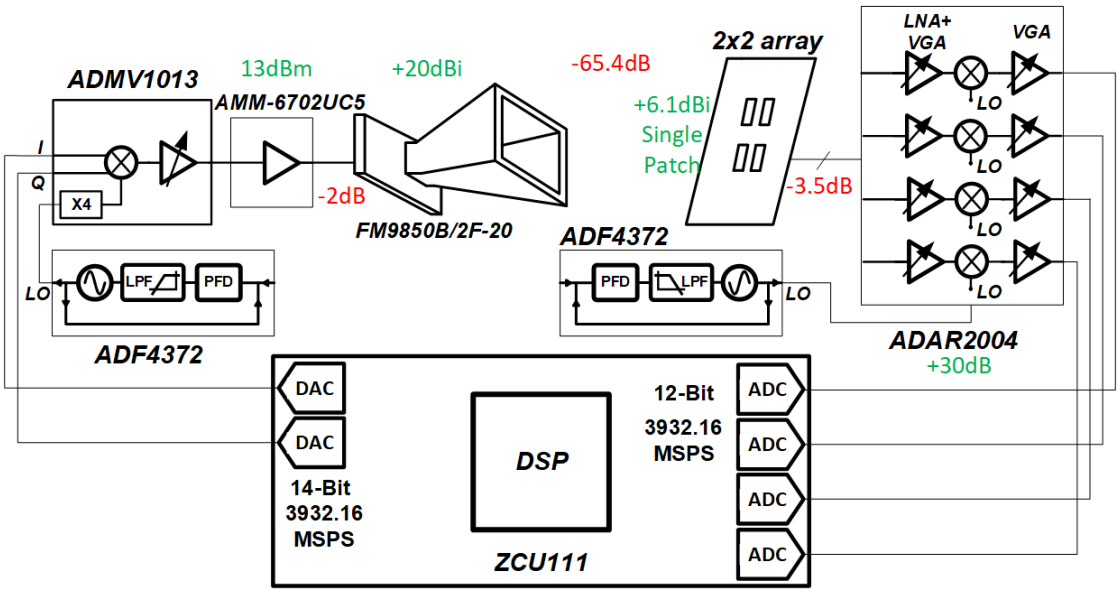

Fig. 2. Block diagram of mm-Wave testbed.

rejection. In the current setup, the image-reject mixer removes the upper sideband by more than 50dB for the entire signal bandwidth. The LO synthesizer, ADI ADF4372, generates a differential 7GHz signal which is fed to LO ports of the ADI ADMV1013. The multiply-by-4 block inside the image-reject mixer raises the LO frequency to 28GHz. Two sidebands at 27.05 GHz and 28.95 GHz are possible so that the lower one reaches the output of the mixer. The resulting mmWave signal is amplified using a mmWave amplifier (AMM-6702UC5), providing 20dB of gain that is applied to a high-gain horn antenna. We operated the amplifier below its 1-dB compression point (P_{1dB}) to ensure that the transmitted signal is not distorted with the PA nonlinearity with the average TX power of 10dBm.

B. 4-Element RX Array

The RX testbed consists of 4-element multi-input-multi-output ADI ADAR2004 followed by four ADCs on ZCU111. Each of the four RX on ADAR2004 comprises of a low-noise amplifier (LNA), a downconversion mixer, a variable gain amplifier (VGA), and an LO synthesizer. Key design considerations for the RX testbed include: a) minimizing gain, delay, and phase mismatch between each channel, and b) elemental access to the downconverted output from each antenna for delay compensation and equalization. A 2x2 custom-designed patch antenna is attached to the array. The received signal by each antenna element in the array is passed to a specific channel of ADAR2004. Similar to ADMV1013, this board also has internal multiply-by-4 to facilitate LO generation and distribution. Another mixer ADF4372 is used to generate the LO signal for the receivers, generating a 7GHz sine wave which is fed to the LO port of ADAR2004, resulting in the down-converted signal mixed back to 950MHz. The VGA in each channel is set to lower the gain mismatches between channels. The IF signal corresponding to each antenna is then digitized using 12-bit high-speed ADCs on ZCU111 for post-processing individual channels. The custom-designed 2x2 patch antenna has differential output ports applied differentially to the ZCU111 optimized for phase- and delay-matching. The differential patch antenna, as shown in Fig. 3 is designed in a multi-layer high-frequency PCB with the third layer driven differentially using a probe-fed structure Fig. 3(a). This structure can be designed such that it shows two resonance frequencies Fig. 3(c). By placing the resonance far enough from each other, wideband performance can be achieved [13]. To account for manufacturing tolerances the antenna is designed to be wide-band. As shown in the return-loss plot, the bandwidth of -12dB is between 26.6-30.75 GHz. This figure also shows the antenna directivity across the aperture angle, θ. At $\theta = 0$, it achieves 6.97dBi. Another important feature of the stacked patch antenna structure is the electrical isolation between the radiating element and RX inputs. Such a feature provides extra protection for the input stages of the RX. Figure 4 shows the mm-Wave testbed with TX-RX distance set to 1.65m (chosen due to lab size constraints). The RX antenna is located on a tripod, allowing its azimuth angle to be controlled precisely using servo motors.

IV. Signal Processing & Calibration on the Received Raw IQ

As shown in the previous section, the four acquired baseband IQ streams from the ZCU board are pre-processed and calibrated to mitigate the impairments and demonstrate the efficacy of the theoretical signal & system model for TTD-based beam training. These steps are summarized in the following subsections.

A. Time & Frequency Synchronization in Baseband

Timing and frequency synchronization are important for OFDM systems. In Section II and [5], a perfect synchronization is assumed. Here, we applied the practical correlation-based 2D-search method [14] for timing synchronization and coarse carrier frequency offset (CFO) estimation, and then applied the conventional cyclic-prefix-based (CP) correlation

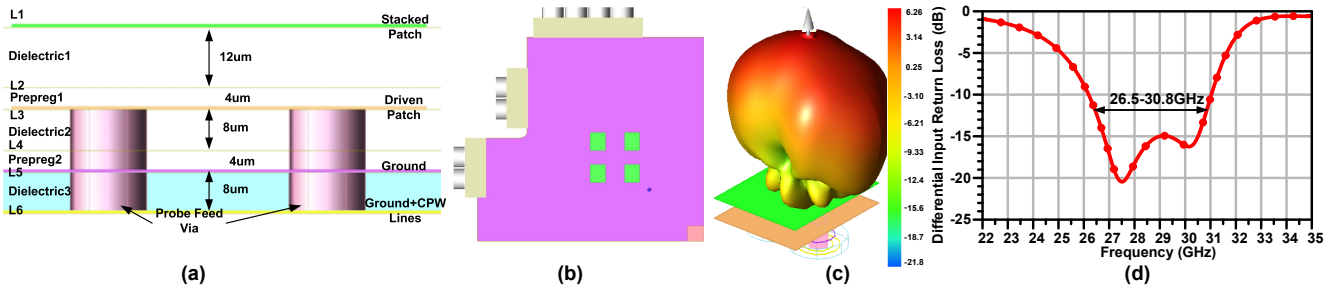

Fig. 3. Differential patch antenna, (a) PCB stack-up, (b) PCB layout of 2x2 array, (c) 3D view of a single patch and its far-field pattern (d) input return loss.

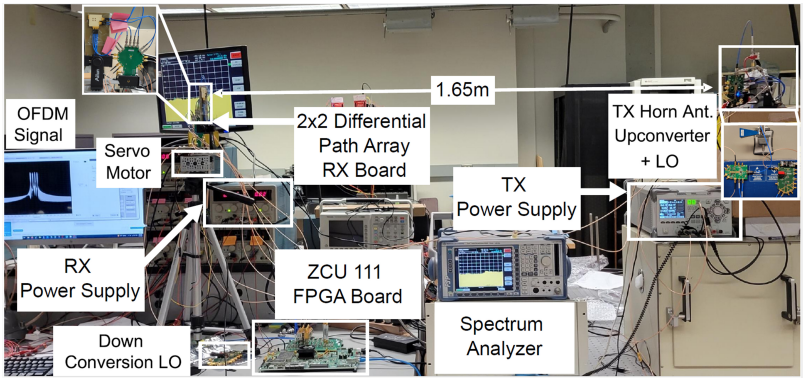

Fig. 4. Photograph of mm-wave beamforming testbed

method [15] for the fine CFO estimation. The transmitter was configured to repeatedly transmit the CP-OFDM pilot symbol, and we made use of the received IQ stream (roughly 10-12 consecutive OFDM symbols length) on the receiver side for synchronization. The coarse CFO estimation in the 2D search allows us to estimate the CFO in a wide range and helps us to finish timing synchronization first. The CP-based fine estimation then gives us a more accurate estimation later.

Figure 5 shows the correlation-based synchronization results. The peaks of the correlation in the time domain show that the transmitted pilots are detected, and the OFDM boundary is synchronized. The peak of the correlation in the frequency domain gives us the estimation of the CFO for later compensation.

B. Removing the Echos & Reflections by OMP-based Reconstruction

Our beam training algorithm in section II relies on the received power on each subcarrier to estimate the AOA. Therefore, if the propagation channel has strong frequency selectivity regardless of AOA, then the proposed algorithm can suffer severe performance degradation. However, when we analyzed the spectrum of the received IQ streams, we observed that the spectrum was non-flat and could even have strong fading in some parts of the band. One possible explanation could be the echoes and reflections in the environment. Therefore, we need to flatten the spectrum of the received IQ streams first before we feed them into the beam training algorithm. In the following, we first tried to get a better understanding of the channel by reconstructing the channel frequency and impulse response. Then, we alleviated the frequency selectivity by reconstructing the signal with a few selected main paths.

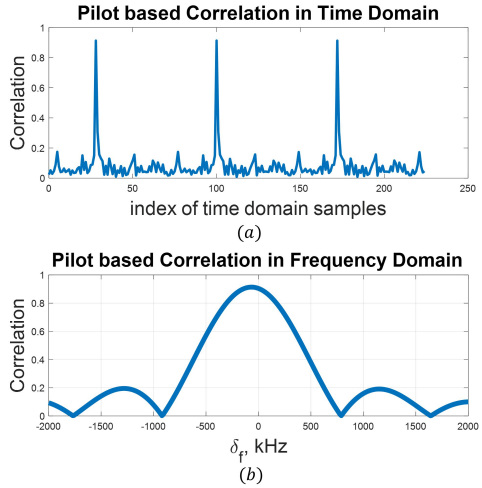

Fig. 5. (a) Correlation with pilots for timing synchronization (b) Correlation with pilots for CFO estimation and compensation

To reconstruct the channel impulse response, we first built a delay-tap dictionary $\mathbf{D}_Q$ with Q atoms, each of which is a delayed version of the transmitted pilots $x_{\text{pilot}}(nT_s)$. We uniformly partitioned the interested delay range $[-T_{cp}, T_{cp}]$ into Q grids and collected them in the ordered set $\mathbb{T}_Q$. The q-th atom in $\mathbf{D}_Q$ is obtained by delaying the transmitted pilot by the q-th element in the set $\mathbb{T}_Q$. Since the delay can be fractional, we implemented the delay with the aid of the FFT-based interpolation. As a result, the q-th atom in the dictionary $\mathbf{D}_Q$ can be expressed as

$$x_q(nT_s) = \text{IFFT}\{\text{FFT}\{x_{\text{pilot}}(nT_s)e^{-j2\pi\Delta t_q n/L_{\text{pilot}}}\}\}, \quad (4)$$

where Δt_q is the q-th element in $\mathbb{T}_Q$, and L_{pilot} is the length of the pilot signal. For the ease of matrix representation, let's

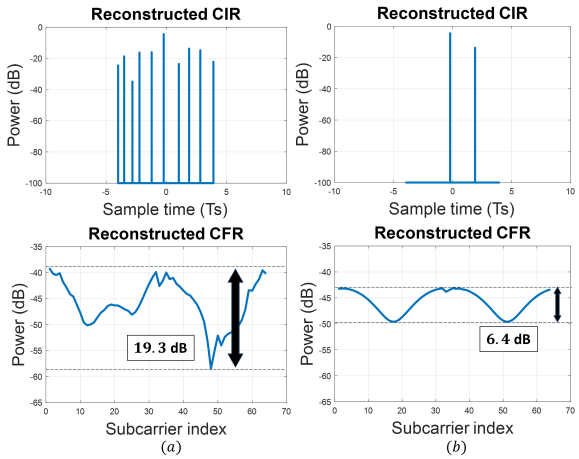

Fig. 6. (a) Channel frequency response (CFR) and channel impulse response (CIR) of the full reconstructed signals from the received raw IQ. All detected paths are included. (b) Channel frequency response (CFR) and channel impulse response (CIR) of the partially reconstructed signal, where the two strongest detected paths are selected.

denote $\mathbf{x}_q = [x_q(0), x_q(1 \cdot T_s), ..., x_q((L_{\text{pilot}} - 1)T_s)]^T \in \mathbb{C}^{L_{\text{pilot}} \times 1}$, $\mathbf{D}_Q = [\mathbf{x}_1, \mathbf{x}_2, ..., \mathbf{x}_Q] \in \mathbb{C}^{L_{\text{pilot}} \times Q}$. Then we can formulate our reconstruction process into the following problem:

$$\min_{\alpha} \parallel \alpha \parallel_0 \quad \text{s.t.} \parallel \mathbf{r} - \mathbf{D}_Q \alpha \parallel_2 \leq \epsilon \tag{5}$$

where $\mathbf{r} = [r(0), r(1 \cdot T_s), ..., r((L_{\text{pilot}} - 1)T_s)]^T \in \mathbb{C}^{L_{\text{pilot}} \times 1}$ is the received IQ after synchronization, $\alpha = [\alpha_1, \alpha_2, ..., \alpha_Q]$. L_0 norm minimization is because of the nature of the sparsity of the mmWave channel. We can see that after (5) is solved, the non-zero elements of α will be the reconstructed channel tap coefficients, and $\mathbf{D}_Q \alpha$ will be the reconstructed signal. The problem in (5) can be treated as a compressive sensing problem, where many algorithms have been proposed in the literature to deal with it. Here, we adopted the orthogonal matching pursuit (OMP) algorithm [16] to solve (5).

Figure 6 (a) shows the OMP-based reconstruction result. The upper figure is the reconstructed channel impulse response, and the lower figure is the measured power at each OFDM subcarrier over the sub-band, which is equivalently the measured power spectrum. We can clearly see that the multipath effect is there, and the resulting power spectrum has strong fading on the right part of the sub-band. To remove this effect, we keep only 1 or 2 strongest paths, equivalently largest values in the reconstructed α, in the reconstructed signal. Figure 6 (b) shows the reconstruction result after removing the multipath effect. Two strongest paths were selected. We can see that the power spectrum is more stable and flat over the whole sub-band.

C. Phase Calibration

Ideally, the array response of a uniform planar array (UPA) $\mathbf{a}_{\text{UPA}}(\theta_{\text{az}}, \theta_{\text{el}})$ can be represented as the Kronecker product of the array responses of the uniform linear array (ULA) in azimuth and elevation planes. However, in reality, the antenna panel and the ADAR board hardware can introduce phase offsets between different antenna elements. To calibrate the phase offsets, we divided our experiment into 2 phases: the calibration phase and the testing phase. In the calibration phase, we ran many tests where the line-of-sight (LOS) angles between the Tx and the Rx are from $-30^0, -20^0, ..., 20^0, 30^0$ in the azimuth plane. We measured the phase differences between antenna elements in these captures and recorded them in our baseline phase calibration dictionary $\mathbf{D}_\theta$. In each scenario in the testing phase, we again measured the phase differences between antenna elements, denoted as $\mathbf{r}_\phi$. Then we can find the θ in the dictionary that matches $\mathbf{r}_\phi$ the most by $\theta_{\text{cal}} = \max_\theta \parallel \mathbf{D}_\theta{}^H \mathbf{r}_\phi \parallel_2$. We then calibrated the $\mathbf{r}_\phi$ with the ideal UPA response $\mathbf{a}_{\text{UPA}}(\theta_{\text{cal}}, \pi)$.

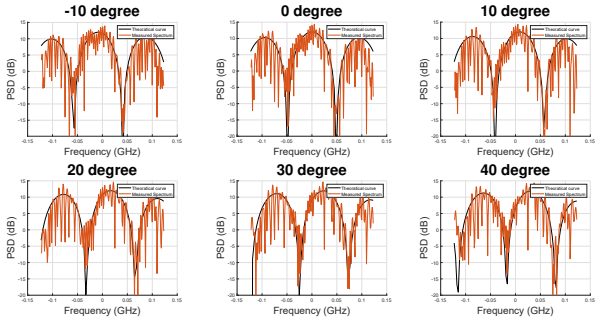

Fig. 7. PSD results of the received baseband signals after digital TTD combination, given different AOAs

There are still a few other potential non-idealities, such as IQ imbalance and phase noise, that were not listed above. Fortunately, we were able to get good demodulation constellations with low EVM ($\approx 0.5\%$) as shown in the fig. 9 without specifically dealing with them. This could indicate that effects from other non-idealities were fairly small in our system.

V. Beam Training Results with OTA Measurement

In this section, we demonstrate our beam training results with our OTA testbed. The transmitted OFDM symbol had FFT size of 64 and CP length of 8. The bandwidth was 245.76 MHz and the subcarrier spacing was 3.84 MHz. The modulation on each subcarrier in a OFDM symbol is BPSK. The baseband OFDM waveform was first upconverted to the IF frequency, then to the mmWave band at 28 GHz. The sampling rate at ADC is 3932.16 MHz. We repetitively transmitted a pilot OFDM symbol so that we have 8 OFDM symbols in one received data capture. We first processed the 4 received IQ streams from the ZCU board with the steps in Section IV to remove the nonidealies. Then we applied the digital TTD of $[0, 0.5T_s, 2.5T_s, 3T_s]$ to each stream from each antenna, and combined then into a single received IQ stream $r_{\text{TTD}(nT_S)}$. Finally, we applied the TTD beam training algorithm in Section II to estimate the AOA.

Figure 7 compares the measured power spectral density (PSD) of the $r_{\text{TTD}(nT_S)}$ with the theoretical PSD derived from (7) in [5], where 6 different AOAs (-10°, 0°, 10°, 20°, 30°, 40°) scenarios were considered. We created different AOAs by using a controllable motor to rotate the receive antenna panel. We can see that the envelope of the measured PSD is pretty aligned with the theoretical PSD curve for all six scenarios, though some distortions are there at the edge of the band. The fact that the measured PSD matches the theoretical PSD is important because the beam training algorithm relies heavily

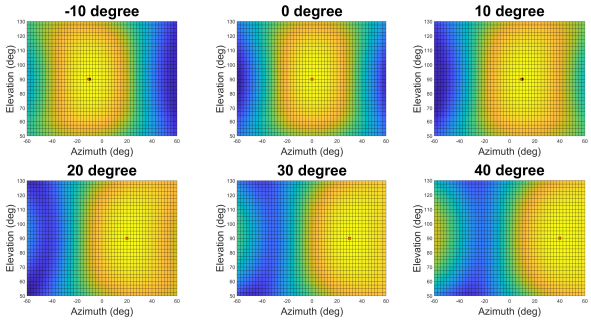

Fig. 8. Heatmap of likelihood of measured PSD for different θ_{az} and θ_{el}

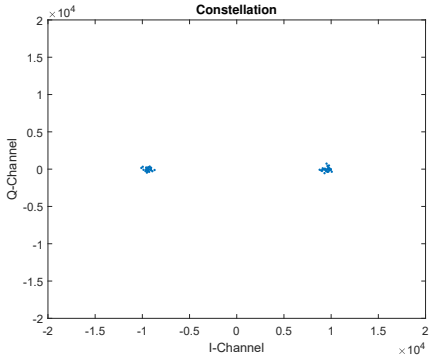

Fig. 9. Constellation plot of the demodulated data

on the correct model of the power on each subcarrier of the received OFDM symbol.

Figure 8 is the heatmap of the correlation between the PSD of $r_{\text{TTD}(nT_S)}$ with that of all the possible atoms in the beam training codebook. Basically, it is a visualization result of the correlation $\frac{\mathbf{p}^H[\mathbf{B}]_{(:,q)}}{||[\mathbf{B}]_{(:,q)}||^2}$ defined in (3). Here, since we only rotate our receive antenna panel in the azimuth plane, and our transmit antenna and receive antenna are on the same horizontal plane, the expected elevation angle is always 90 degrees. The black dot is the ground truth angle, and the red dot is the estimated angle. In most of the scenarios (where ground truth AOAs are $0, 20, 30,$ and 40 degree), the black dots overlapped with the red dots, which means that we got perfect estimation results. In the scenarios where ground truth AOAs are -10 and 10 degree, we measure 1° error estimation, which is fairly small.

Figure 9 is the constellation diagram of the demodulated received IQ streams. Because the BPSK symbols are applied to all the subcarriers, the separated 2 clusters of points are expected. The clean separation of the constellation shows that with the correct synchronization and equalization process, the communication link was properly established.

VI. Conclusions and Future Work

This paper is the first work to demonstrate the TTD-based 3D beam training algorithm in an OTA testbed. By integrating several COTS RF modules with Xilinx RFSoC-based data acquisition, an mmWave transceiver system was built to verify the 3D beam training algorithm in OTA tests. After the nonidealities were compensated by the proposed algorithm/calibration, the post-processing experimental result on a 2×2 uniform planar array accurately estimated the incident azimuth and elevation angles with 50% coverage efficiency. A larger number of antennas and integration with analog TTD chips exhibiting longer delay range-to-resolution ratios are planned as future work for more practical system verification.

References

[1] R. W. Heath, N. González-Prelcic, S. Rangan, W. Roh, and A. M. Sayeed, "An overview of signal processing techniques for millimeter wave mimo systems," *IEEE Journal of Selected Topics in Signal Processing*, vol. 10, no. 3, pp. 436–453, 2016.

[2] V. Boljanovic, H. Yan, E. Ghaderi, D. Heo, S. Gupta, and D. Cabric, "Design of millimeter-wave single-shot beam training for true-time-delay array," in *2020 IEEE 21st International Workshop on Signal Processing Advances in Wireless Communications (SPAWC)*, 2020, pp. 1–5.

[3] C.-C. Lin, V. Boljanovic, H. Yan, E. Ghaderi, M. A. Mokri, J. J. Gaddis, A. Wadaskar, C. Puglisi, S. Mohapatra, Q. Xu, S. Poolakkal, D. Heo, S. Gupta, and D. Cabric, "Wideband beamforming with rainbow beam training using reconfigurable true-time-delay arrays for millimeter-wave wireless [feature]," *IEEE Circuits and Systems Magazine*, vol. 22, no. 4, pp. 6–25, 2022.

[4] E. Ghaderi, A. Sivadhasan Ramani, A. A. Rahimi, D. Heo, S. Shekhar, and S. Gupta, "An integrated discrete-time delay-compensating technique for large-array beamformers," *IEEE Transactions on Circuits and Systems I: Regular Papers*, vol. 66, no. 9, pp. 3296–3306, 2019.

[5] A. Wadaskar, V. Boljanovic, H. Yan, and D. Cabric, "3d rainbow beam design for fast beam training with true-time-delay arrays in wideband millimeter-wave systems," in *2021 55th Asilomar Conference on Signals, Systems, and Computers*, 2021, pp. 85–92.

[6] Q. Xu, A. Wadaskar, C.-C. Lin, H. Yan, V. Boljanovic, S. Gupta, and D. Cabric, "A switching-less true-time-delay-based beam probing approach for ultra-low latency wireless communications: System analysis and demonstration," *IEEE Transactions on Circuits and Systems II: Express Briefs*, vol. 69, no. 10, pp. 4113–4117, 2022.

[7] V. Boljanovic, H. Yan, C.-C. Lin, S. Mohapatra, D. Heo, S. Gupta, and D. Cabric, "Fast beam training with true-time-delay arrays in wideband millimeter-wave systems," *IEEE Transactions on Circuits and Systems I: Regular Papers*, vol. 68, no. 4, pp. 1727–1739, 2021.

[8] H. Yan, V. Boljanovic, and D. Cabric, "Wideband millimeter-wave beam training with true-time-delay array architecture," in *2019 53rd Asilomar Conference on Signals, Systems, and Computers*, 2019, pp. 1447–1452.

[9] A. Devices, *24 GHz to 29.5 GHz Transmitter/Receiver, Dual Polarization Beamformer*, 2022. [Online]. Available: https://www.analog.com/en/products/admv4821.html

[10] Renesas, *28GHz 8-Channel, Half-Duplex Transceiver IC*, 2023. [Online]. Available: https://www.renesas.com/us/en/document/sds/f5288-short-form-datasheet?r=1050916

[11] ——, *8-Channel Transmit Active Beamforming IC for Ka-Band SATCOM*, 2021. [Online]. Available: https://www.renesas.com/us/en/products/rf-products/phased-array-beamformers/f6522-8-channel-transmit-active-beamforming-ic-ka-band-satcom

[12] PSemi, *8-channel Beamforming Front End, 24.25–27.5 GHz*, 2022. [Online]. Available: https://www.psemi.com/pdf/datasheets/pe188100pb.pdf

[13] R. Waterhouse, "Design of probe-fed stacked patches," *IEEE Transactions on Antennas and Propagation*, vol. 47, no. 12, pp. 1780–1784, 1999.

[14] D. Wang, Z. Mei, H. Zhang, and H. Li, "A novel pss timing synchronization algorithm for cell search in 5g nr system," *IEEE Access*, vol. 9, pp. 5870–5880, 2021.

[15] J. van de Beek, M. Sandell, and P. Borjesson, "Ml estimation of time and frequency offset in ofdm systems," *IEEE Transactions on Signal Processing*, vol. 45, no. 7, pp. 1800–1805, 1997.

[16] T. T. Cai and L. Wang, "Orthogonal matching pursuit for sparse signal recovery with noise," *IEEE Transactions on Information Theory*, vol. 57, no. 7, pp. 4680–4688, 2011.